Simulations of Raman Spectra Using the Fragment Molecular Orbital Method

Hiroya Nakata,*,[†,‡,#] Dmitri G. Fedorov,*,[§] Satoshi Yokojima,[∥,‡] Kazuo Kitaura,[⊥] and Shinichiro Nakamura[‡]

[†]Department of Biomolecular Engineering, Tokyo Institute of Technology, 4259 Nagatsuta-cho, Midori-ku, Yokohama, Kanagawa 226-8501, Japan

[‡]Nakamura Lab, Research Cluster for Innovation, 2-1 Hirosawa, Wako, Saitama 351-0198, Japan

[§]NRI, National Institute of Advanced Industrial Science and Technology (AIST), 1-1-1 Umezono,Tsukuba, Ibaraki 305-8568, Japan

[∥]Tokyo University of Pharmacy and Life Sciences, 1432-1 Horinouchi, Hachiouji-shi, Tokyo 192-0392, Japan

[⊥]Graduate School of System Informatics, Kobe University, 1-1 Rokkodai-cho, Nada-ku, Kobe 657-8501 Japan

[#]Japan Society for the Promotion of Science, Kojimachi Business Center Building, 5-3-1 Kojimachi, Chiyoda-ku, Tokyo 102-0083, Japan

Ⓢ Supporting Information

ABSTRACT: We developed an approach to calculate normal Raman activities based on the fragment molecular orbital method. For this purpose, we derived the FMO gradient and coupled-perturbed Hartree–Fock equations in the presence of the static electric field. The accuracy is evaluated in comparison with full ab initio calculations for a set of closed-shell and radical systems. We applied the method to calculate Raman and IR spectra of a polystyrene oligomer and crambin (PDB: 1CRN) and performed an assignment of peaks based on localized normal modes. The computational timings demonstrate the efficiency of the method.
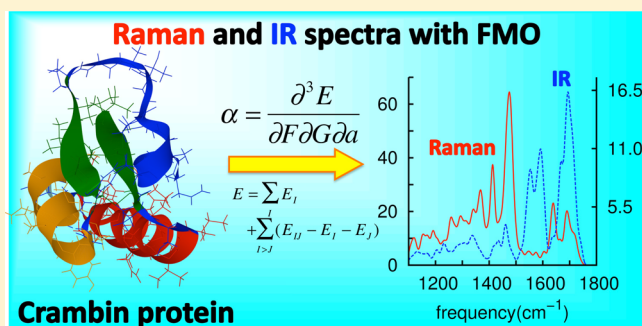
1. INTRODUCTION

Vibrational infrared (IR)[1] and Raman[2,3] spectroscopies play an important role in chemistry. Quantum mechanical (QM) simulations of infrared and Raman spectra require the second derivative of the energy (the Hessian) with respect to nuclear coordinates.[4−6] Reducing high computational cost, various alternatives to full ab initio calculations of the Hessian are available such as combined QM and molecular mechanics (QM/MM),[7,8] our own n-layered integrated molecular orbital and molecular mechanics (ONIOM) method,[9] and density functional based tight binding (DFTB).[10] It is also possible to evaluate the Hessian numerically, usually using analytic energy gradients, which can also be done for a subset of atoms.[11−13]

A calculation of IR intensities or Raman activities requires derivatives of both dipole moment and polarizability tensor with respect to normal vibrational coordinates. The latter derivative is the third derivative of the energy, and it can be calculated for Hartree–Fock[14,15] and density functional theory.[16,17] Ab initio Raman calculations have been conducted for polypeptides representing biological systems.[18−20] There are various efficient quantum-mechanical methods such as semiempirical approaches,[21,22] linear-scaling algorithms,[23,24] and fragment-based methods.[25−37] However, analytic second derivatives are available only for a few of these methods.[38−42]

For the fragment molecular orbital (FMO) method[43−47] the analytic first[48,49] and second[42,50] derivatives of the energy have been developed. Dynamic polarizabilities can also be calculated.[51] FMO has been applied to a variety of molecules including proteins,[52,53] DNA,[54] and inorganic systems.[55−59]

In this work, we develop a method to simulate Raman spectra with FMO using both restricted[43] and unrestricted[60,61] Hartree–Fock (HF). We use the notation of HF throughout this work when we mean either RHF or UHF. Because the dispersion interaction is very important in chemistry, we employ the Grimme's empirical dispersion energy.[62,63] To the best of our knowledge, the analytic second derivative for this dispersion model has not been published, and we derive it in this work. We also derive the coupled-perturbed Hartree–Fock (CPHF) equations[64] under the electric field perturbation in the framework of FMO and use them to obtain the third derivatives of the energy necessary for Raman activities.

The accuracy of Raman spectra computed with FMO is evaluated for vitamin C[65] and α-tocopherol[66] (vitamin E) for closed-shell restricted HF (RHF) and 2,2,6,6-tetramethylpiperidine 1-oxyl (TEMPO) for open-shell unrestricted HF (UHF). The computational efficiency is demonstrated for water

clusters. We apply our developed method to a polystyrene oligomer and crambin (PDB: 1CRN)[67] and discuss insights into the Raman spectra of large systems provided by FMO.

2. THEORY

2.1. FMO Summary. In FMO, the system is divided into fragments (also called monomers), which are calculated in the embedding electrostatic potential (ESP), obtained from the density of all fragments. These monomer calculations are repeated iteratively until convergence, followed by the calculation of fragment pairs (dimers) in the presence of ESP. More details can be found elsewhere.[42] The total energy in FMO is expanded in the many-body series,[68,69] and in this work we use the two-body expansion (FMO2).

The total energy E in FMO2 is

$$E^{\mathrm{FMO2}} = \sum_I^N E_I' + \sum_{I>J}^N (E_{IJ}' - E_I' - E_J') + \sum_{I>J}^N \mathrm{Tr}(\Delta\mathbf{D}^{IJ}\mathbf{V}^{IJ}) \tag{1}$$

where E_X' the internal fragment energy of fragment X ($X = I$ or IJ). N is the number of fragments. The internal energies are obtained from self-consistent field (SCF) energies E_X after SCF converges by subtracting the interaction with the embedding potential (ESP) $\mathbf{V}^X$ as

$$E_X' = E_X - \mathrm{Tr}(\mathbf{D}^X\mathbf{V}^X) \tag{2}$$

where $\mathbf{D}^X$ is the density matrix of X and

$$V_{\mu\nu}^X = \sum_{K\neq X}^N (u_{\mu\nu}^K + v_{\mu\nu}^K) \tag{3}$$

The one-electron u and two-electron v integrals are

$$u_{\mu\nu}^K = \sum_{A\in K} \left\langle \mu \left| \frac{-Z_A}{|\mathbf{r} - \mathbf{R}_A|} \right| \nu \right\rangle \tag{4}$$

$$v_{\mu\nu}^K = \sum_{\lambda\sigma\in K} D_{\lambda\sigma}^K (\mu\nu|\lambda\sigma) \tag{5}$$

where $\mathbf{R}_A$ and Z_A are the coordinates and nuclear charge of atom A, respectively. A, B, and C are used to label atoms, while Greek indices are used for atomic orbitals. $(\mu\nu|\lambda\sigma)$ is the two-electron integral in atomic orbital basis. $\Delta\mathbf{D}^{IJ}$ is the difference between the electron density matrix of dimer IJ and the sum of the densities of monomers I and J.

The second derivative of the energy in eq 1 with respect to the nuclear coordinates a and b is (more details are given elsewhere[42]),

$$\frac{\partial^2 E^{\mathrm{FMO2}}}{\partial a \partial b} = \sum_I^N \frac{\partial^2 E_I'}{\partial a \partial b} + \sum_{I>J}^N \left(\frac{\partial^2 E_{IJ}'}{\partial a \partial b} - \frac{\partial^2 E_I'}{\partial a \partial b} - \frac{\partial^2 E_J'}{\partial a \partial b} \right)$$
$$+ \sum_{I>J}^N \frac{\partial^2 \mathrm{Tr}(\Delta\mathbf{D}^{IJ}\mathbf{V}^{IJ})}{\partial a \partial b} \tag{6}$$

The second derivative of the internal energy E_X' is

$$\frac{\partial^2 E_X'}{\partial a \partial b} = \frac{\partial^2 E_X'^{\mathrm{HF}}}{\partial a \partial b} + \frac{\partial^2 E_X^{\mathrm{dis}}}{\partial a \partial b} - \bar{U}^{ab,X} \tag{7}$$

where E_X^{HF} and E_X^{dis} are the HF and dispersion energies, respectively, and $\bar{U}^{ab,X}$ is the Hessian contribution arising from the orbital responses related to the derivative of MO

coefficients in ESP. These responses are FMO-specific terms, whereas HF Hessians are calculated for fragments and their pairs as in regular RHF (UHF) calculations. In order to obtain the response terms, CPHF equations have to be solved.[42] The second derivatives of the dispersion terms in eq 7 are derived in this work (see below).

2.2. Raman Activity Calculation. The normal Raman activity[14,15] of a vibrational mode i is

$$J_i = 45\alpha_i'^2 + 7\gamma_i'^2 \tag{8}$$

The symmetric contribution α_i' is defined as

$$\alpha_i' = \frac{1}{3}\left[\left(\frac{\partial\alpha_{xx}}{\partial Q_i}\right) + \left(\frac{\partial\alpha_{yy}}{\partial Q_i}\right) + \left(\frac{\partial\alpha_{zz}}{\partial Q_i}\right) \right] \tag{9}$$

The polarizability tensor α_{xy} is the second derivative of the energy with respect to the external electric fields $\mathcal{F}_x$ and $\mathcal{F}_y$

$$\alpha_{xy} = \frac{\partial^2 E}{\partial\mathcal{F}_x\partial\mathcal{F}_y} \tag{10}$$

and $\partial\alpha_{xy}/\partial Q_i$ is the derivative of the polarizability tensor with respect to a normal coordinate Q_i, which is a linear combination of atomic coordinates.

$$Q_i = \sum_{a=1}^{3M} l_{ai}a \tag{11}$$

where a is a Cartesian coordinate of an atom, M is the number of atoms, and l_{ai} is the eigenvector of the Hessian for the normal mode i. The polarizability tensor derivatives $\partial\alpha_{xy}/\partial Q_i$ are obtained from the Cartesian derivative $\partial\alpha_{xy}/\partial a$ as

$$\frac{\partial\alpha_{xy}}{\partial Q_i} = \sum_{a=1}^{3M} l_{ai}\frac{\partial\alpha_{xy}}{\partial a} \tag{12}$$

The anisotropic derivative contribution γ_i' is defined as

$$\gamma_i'^2 = \frac{1}{2}\left[\left(\frac{\partial\alpha_{xx}}{\partial Q_i} - \frac{\partial\alpha_{yy}}{\partial Q_i}\right)^2 + \left(\frac{\partial\alpha_{yy}}{\partial Q_i} - \frac{\partial\alpha_{zz}}{\partial Q_i}\right)^2 \right.$$
$$\left. + \left(\frac{\partial\alpha_{zz}}{\partial Q_i} - \frac{\partial\alpha_{xx}}{\partial Q_i}\right)^2 + 6\left\{ \left(\frac{\partial\alpha_{xy}}{\partial Q_i}\right)^2 + \left(\frac{\partial\alpha_{yz}}{\partial Q_i}\right)^2 + \left(\frac{\partial\alpha_{zx}}{\partial Q_i}\right)^2 \right\} \right] \tag{13}$$

In order to obtain normal coordinates associated with vibrational frequencies, it is necessary to calculate the second derivatives of the energy with respect to nuclear coordinates a and b and transform them into mass-weighted Cartesian coordinates using atomic masses m_a:

$$H_{ab}' = \frac{\partial^2 E}{\partial a \partial b} \Big/ \sqrt{m_a m_b} \tag{14}$$

By diagonalizing the mass-weighted Hessian matrix $\mathbf{H}'$, one obtains the vibrational frequencies and the normal coordinates as its eigenvalues and eigenvectors, respectively. To calculate the Raman activity, one has to obtain both the Hessian matrix in eq 14 and the third derivative of the energy with respect to pairs of the electric field components $\mathcal{F}$ and a nuclear coordinate a.

2.3. Second Derivative of the Dispersion Energy. There are the original[62] and modified[63] formulations of the dispersion (dis) energy, which we denote by D2 and D3,

respectively. Both of them are completely independent of the electronic state, and thus their addition is not coupled to it in any way. The first and second derivatives of the dispersion energy are added to the corresponding electronic contributions.

$$E_{dis}^{D2} = -s_6 \sum_{A,B} \frac{C_6^{AB}}{R_{AB}^6} f_{d,6}^{D2}(R_{AB}) \tag{15}$$

$$E_{dis}^{D3} = - \sum_{n=6,8,10} \sum_{A,B} s_n \frac{C_n^{AB}}{R_{AB}^n} f_{d,n}^{D3}(R_{AB}) \\ - \sum_{A,B,C} f_{d,3}^{D3}(\bar{R}_{ABC}) E^{ABC} \tag{16}$$

where C_n^{AB} denotes the averaged n-order dispersion coefficient for an atomic pair AB. R_{AB} and $\bar{R}_{ABC}$ are the pairwise and averaged (over three pairs) internuclear distances, respectively. s_n is a scale factor (a parameter). $f_{d,6}^{D2}(R_{AB})$ and $f_{d,n}^{D3}(R_{AB})$ are the damping functions:

$$f_{d,6}^{D2}(R_{AB}) = \frac{1}{1 + \exp(-dR_{AB}/(s_R R_{AB}^0) - 1)} \tag{17}$$

$$f_{d,n}^{D3}(R_{AB}) = \frac{1}{1 + 6(R_{AB}/(s_{R,n} R_{AB}^0))^{-\alpha_n}} \tag{18}$$

where R_{AB}^0 is the sum of the atomic van der Waals radii derived from ab initio calculations[70] and scaled by the factor of 1.1, s_R and $s_{R,n}$ are the multipliers for the van der Waals radii, d is a damping factor, and α_n are integer parameters: $\alpha_3 = 16$, $\alpha_6 = 14$, and for $n > 6$, $\alpha_{n+2} = \alpha_n + 2$. The third-order energy for three atoms ABC is

$$E^{ABC} = \frac{C_9^{ABC}(3\cos\theta_a \cos\theta_b \cos\theta_c + 1)}{(R_{AB}R_{BC}R_{CA})^3} \tag{19}$$

where θ_a, θ_b, and θ_c are the angles in the triangle formed by the three atoms A, B, and C. C_9^{ABC} is the triple-dipole constant.

The analytic second derivative of E_{dis}^{D2} is

$$\frac{\partial^2 E_{dis}^{D2}}{\partial a \partial b} = -\sum_A \sum_B s_6 C_6^{AB} \left[\frac{\partial \Delta R_{AB,\{a\}}}{\partial a} \frac{\partial \Delta R_{AB,\{b\}}}{\partial b} \right.$$
$$\times \left(\frac{d}{s_R R_{AB}^0} (f_{d,6}^{D2})^2 \exp\left[-\frac{dR_{AB}}{s_R R_{AB}^0} - 1 \right] \frac{1}{R_{AB}^7} - 6\frac{f_{d,6}^{D2}}{R_{AB}^8} \right)$$
$$+ \frac{2d}{s_R R_{AB}^0} \exp\left[-\frac{dR_{AB}}{s_R R_{AB}^0} - 1 \right] \frac{f_{d,6}^{D2}}{R_{AB}^7} \frac{\partial f_{d,6}^{D2}}{\partial b} \Delta R_{AB,\{a\}} \frac{\partial \Delta R_{AB,\{a\}}}{\partial a}$$
$$+ \frac{d}{s_R R_{AB}^0} \frac{\partial\left(\exp\left[-\frac{dR_{AB}}{s_R R_{AB}^0} - 1 \right] \right)}{\partial b} \frac{(f_{d,6}^{D2})^2}{R_{AB}^7} \Delta R_{AB,\{a\}} \frac{\partial \Delta R_{AB,\{a\}}}{\partial a}$$
$$- 7\frac{d}{s_R R_{AB}^0} (f_{d,6}^{D2})^2 \exp\left[-\frac{dR_{AB}}{s_R R_{AB}^0} - 1 \right] \frac{1}{R_{AB}^9}$$
$$\times \Delta R_{AB,\{a\}} \Delta R_{AB,\{b\}} \frac{\partial \Delta R_{AB,\{a\}}}{\partial a} \frac{\partial \Delta R_{AB,\{b\}}}{\partial b}$$
$$- 6\frac{\partial f_{d,6}^{D2}}{\partial b} \frac{\Delta R_{AB,\{a\}}}{R_{AB}^8} \frac{\partial \Delta R_{AB,\{a\}}}{\partial a} + 48\frac{f_{d,6}^{D2}}{R_{AB}^{10}} \Delta R_{AB,\{a\}} \Delta R_{AB,\{b\}}$$
$$\left. \times \frac{\partial \Delta R_{AB,\{a\}}}{\partial a} \frac{\partial \Delta R_{AB,\{b\}}}{\partial b} \right] \tag{20}$$

where $\Delta R_{AB,\{a\}}$ denotes the difference in a specific Cartesian coordinate (not the interatomic distance). An atomic coordinate a (from 1 to $3M$) corresponds to atom C_a (from 1 to M) with the Cartesian coordinate component p_a (where $p_a = x,y,z$).

$$\Delta R_{AB,\{a\}} = R_{A,p_a} - R_{B,p_a} \tag{21}$$

where R_{A,p_a} is the p_a Cartesian component of the coordinate of atom A. It is convenient to calculate the derivatives of $f_{d,6}^{D2}$ and $\exp(-dR_{AB}/(s_R R_{AB}^0) - 1)$ first and then evaluate the second derivative of E_{dis}^{D2}. See Supporting Information for more details on the derivation of eq 20.

We verified that the analytic second derivative of E_{dis}^{D2} is correct by comparing the results to numeric derivatives. We did not develop the analytic second derivative for E_{dis}^{D3} in this study. Instead, we calculate numeric second derivatives for it, using analytic first derivatives. Such an implementation is general and can be used for any future modifications of the dispersion energy.

2.4. Derivative of the Polarizability Tensor. The derivative of the polarizability tensor α is the third derivative of the energy with respect to a coordinate a and two components of the electric field $\mathcal{F}_i$ ($i = x,y$ and z). We obtain it by calculating the energy gradient in the presence of the electric field and differentiating this gradient numerically twice (double differencing[14,15] for $\mathcal{F}_x\mathcal{F}_x$, $\mathcal{F}_y\mathcal{F}_y$, $\mathcal{F}_z\mathcal{F}_z$, $\mathcal{F}_x\mathcal{F}_y$, $\mathcal{F}_y\mathcal{F}_z$, and $\mathcal{F}_z\mathcal{F}_x$). In total, 19 single point energy gradient calculations are necessary, varying these fields (1 for no field, 6 for the symmetric terms such as $\mathcal{F}_x\mathcal{F}_x$ and 12 for the asymmetric terms such as $\mathcal{F}_x\mathcal{F}_y$). All fragment calculations in this subsection are performed with the field included, so that for instance, $\mathbf{D}^{IJ}$ is the density matrix of fragment IJ, calculated with the field. Also, all explicit derivations below are provided for RHF, and we omit the corresponding UHF equations.

In FMO, the energy gradient in the presence of the electric field $\mathcal{F}$ is

$$\frac{\partial E}{\partial a} = \sum_I^N \frac{\partial E_I'}{\partial a} + \sum_{I>J}^N \left(\frac{\partial E_{IJ}'}{\partial a} - \frac{\partial E_I'}{\partial a} - \frac{\partial E_J'}{\partial a} \right) \\ + \sum_{I>J}^N \frac{\partial \mathrm{Tr}(\Delta \mathbf{D}^{IJ} \mathbf{V}^{IJ})}{\partial a} \tag{22}$$

and the derivative of the internal fragment energy is

$$\frac{\partial E_X'}{\partial a} = \sum_{\mu\nu \in X} D_{\mu\nu}^X h_{\mu\nu}^{a,X} + \sum_{\mu\nu \in X} D_{\mu\nu}^X P_{\mu\nu}^{a,X} \\ + \frac{1}{2}\left[D_{\mu\nu}^X D_{\lambda\sigma}^X - \frac{1}{2}D_{\mu\lambda}^X D_{\nu\sigma}^X \right](\mu\nu|\lambda\sigma)^a \\ + \sum_{\mu\nu \in X} D_{\mu\nu}^X \mathcal{F}\cdot(\mu|\hat{\mu}^0|\nu)^a - 2\sum_{ij \in X}^{occ} S_{ij}^{a,X} F_{ji}'^X - \bar{U}^{a,X,X} \\ + \frac{\partial E_X^{NR}}{\partial a} \tag{23}$$

where $F_{ji}'^X$, $S_{ij}^{a,X}$, and E_X^{NR} are the internal Fock matrix elements (related to the full Fock matrix as $F_{ji}^X = F_{ji}'^X + V_{ji}^X$), the derivative overlap integrals, and the nuclear repulsion energy of fragment X, respectively.

The $\hat{\mu}^0$ is the permanent dipole moment operator, and $\bar{U}^{a,X,Y}$ is defined as

3691

dx.doi.org/10.1021/ct5003829 | J. Chem. Theory Comput. 2014, 10, 3689–3698

$$\bar{U}^{a,X,Y} = 4 \sum_{i \in X}^{occ} \sum_{r \in Y}^{vir} U_{ri}^{a,X} V_{ri}^{Y} \tag{24}$$

where $U_{ri}^{a,X}$ are the response terms related to the change in the MO coefficients with respect to a change in nuclear coordinates. The ESP of X in MO basis

$$V_{ri}^{X} = \sum_{\mu\nu \in X} C_{\mu r}^{X*} C_{\nu i}^{X} V_{\mu\nu}^{X} \tag{25}$$

where $C_{\mu r}^{X}$ are the expansion coefficients of MO i in the basis of AOs μ, in fragment X. Throughout, $i,j,k,$ and l denote occupied molecular orbitals, while r is a virtual molecular orbital. The h denotes the one-electron core Hamiltonian, whereas P is the projection operator used to divide the AO space for atoms at the fragment border.[71]

The differentiation of the embedded density difference term in eq 22 gives

$$\frac{\partial \text{Tr}(\Delta \mathbf{D}^{IJ} \mathbf{V}^{IJ})}{\partial a} = \sum_{\mu\nu \in IJ} \frac{\partial (D_{\mu\nu}^{IJ} V_{\mu\nu}^{IJ})}{\partial a} - \sum_{\mu\nu \in I} \frac{\partial (D_{\mu\nu}^{I} V_{\mu\nu}^{IJ})}{\partial a} - \sum_{\mu\nu \in J} \frac{\partial (D_{\mu\nu}^{J} V_{\mu\nu}^{IJ})}{\partial a} \tag{26}$$

$$\sum_{\mu\nu \in X} \frac{\partial (D_{\mu\nu}^{X} V_{\mu\nu}^{IJ})}{\partial a} = 2 \sum_{i \in X}^{occ} V_{ii}^{a,IJ} + 4 \sum_{r \in X}^{vir} \sum_{i \in X}^{occ} U_{ri}^{a,X} V_{ri}^{IJ} + 8 \sum_{k \in IJ} \sum_{K \neq I,J} \sum_{r \in K}^{vir} \sum_{i \in K}^{occ} U_{ri}^{a,K} (kk|ri) \tag{27}$$

where the derivative ESP in MO basis is

$$V_{ri}^{a,IJ} = \sum_{\mu\nu \in IJ} C_{\mu r}^{IJ*} C_{\nu i}^{IJ} V_{\mu\nu}^{a,IJ} \tag{28}$$

The derivative ESP in AO basis is

$$V_{\mu\nu}^{a,IJ} = \sum_{K \neq I,J}^{N} \left[\sum_{A \in K} \left\langle \mu \left| \frac{-Z_A}{|\mathbf{r} - \mathbf{R}_A|} \right| \nu \right\rangle^{a} + \sum_{\lambda,\sigma \in K} D_{\lambda\sigma}^{K} (\mu\nu|\lambda\sigma)^{a} \right] \tag{29}$$

Inserting eqs 23 and 26 into eq 22, one can obtain the analytic energy gradient in the presence of the electric field $\mathcal{F}$, for which one has to calculate the response terms $U_{ri}^{a,K}$. Therefore, solving CPHF equations is necessary with the inclusion of the external electric field $\mathcal{F}$.

2.5. CPHF Equations for the Electric Field. For the FMO energy gradient in both RHF and UHF, the first-order CPHF equations involve only monomer response terms (i.e., no dimer responses).[48,60] The CPHF equations are obtained from the derivative of the Fock matrix in the presence of electric field $\mathcal{F}$ with respect to a nuclear coordinate a.

$$\frac{\partial F_{ij}^{I}}{\partial a} = F_{ij}^{a,I} - (\epsilon_{j}^{I} - \epsilon_{i}^{I}) U_{ij}^{a,I} - \frac{1}{2} \sum_{k \in I}^{occ} \sum_{l \in I}^{occ} S_{kl}^{a,I} A'_{ij,kl}$$
$$+ \sum_{r \in I}^{vir} \sum_{k \in I}^{occ} U_{rk}^{a,I} A'_{ij,rk} + \frac{1}{2} \sum_{K \neq I} \sum_{k \in K}^{occ} \sum_{l \in K}^{occ} S_{kl}^{a,K} A_{ij,kl}^{I,K}$$
$$- \sum_{K \neq I} \sum_{r \in K}^{vir} \sum_{k \in K}^{occ} U_{rk}^{a,K} A_{ij,rk}^{I,K} \tag{30}$$

where ϵ_{i}^{X} is the energy of MO i in fragment X, $S_{kl}^{a,K}$ are the derivatives of overlap integrals. The off-diagonal part of the orbital Hessian $A_{ij,kl}^{I,K}$ is

$$A_{ij,kl}^{I,K} = -4(ij|kl) \tag{31}$$

where $(ij|kl)$ is a two-electron integral in MO basis and the integral derivative contribution to the Fock matrix gradient is

$$F_{ij}^{a,I} = h_{ij}^{a,I} + V_{ij}^{a,I} + P_{ij}^{a,I} + \mathcal{F} \cdot (i|\hat{\mu}^{0}|j)^{a}$$
$$+ \sum_{k \in I}^{occ} [2(ij|kk)^{a} - (ik|jk)^{a}] \tag{32}$$

Using the relationship of $\partial F_{ij}^{I}/\partial a = 0$ for $i \neq j$ because of the diagonality, one obtains the CPHF equation in the presence of the electric field $\mathcal{F}$:

$$\mathbf{B}_{0}^{a} = \mathbf{AU} \tag{33}$$

where the diagonal block of the matrix $\mathbf{A}$ for fragment I is

$$A_{ij,kl}^{I,I} = \delta_{ik}\delta_{jl}(\epsilon_{j}^{I} - \epsilon_{i}^{I}) - A'_{ij,kl} \tag{34}$$

$$A'_{ij,kl} = 4(ij|kl) - (ik|jl) - (il|jk) \tag{35}$$

The components of $\mathbf{B}_{0}^{a}$ are

$$B_{0,ij}^{a,I} = F_{ij}^{a,I} - S_{ij}^{a,I} \epsilon_{j}^{I} - \sum_{k \in I}^{occ} \sum_{l \in I}^{occ} S_{kl}^{a,I} [2(ij|kl) - (ik|jl)]$$
$$- \sum_{K \neq I} \sum_{k \in K}^{occ} \sum_{l \in K}^{occ} 2S_{kl}^{a,K} (ij|kl) \tag{36}$$

Compared to the FMO gradient without the field, the necessary modification of the CPHF equations is the addition of the derivative of the dipole moment, $\mathcal{F} \cdot (i|\hat{\mu}^{0}|j)^{a}$ in eq 32. The CPHF equations are solved using the Z-vector method.[64]

Summarizing, for the normal Raman activity in eq 8, one has to perform geometry optimization, calculate the Hessian and do normal vibrational analysis, and then evaluate the polarizability tensor α according to eqs 9 and 13. In this work we used the most recent formulation of the Grimme's dispersion energy[63] available in GAMESS, and because of the triatomic terms (see eq 16), we numerically differentiated analytic derivatives of the dispersion energy, although we also implemented the analytic second derivative for the earlier version of the dispersion energy[62] in eq 15. The third derivative of the polarizability tensor α is numerically obtained by performing 19 energy gradient calculations in the presence of the electric field, for which it is necessary to use eqs 23, 32, and 36. The CPHF equations are solved using the conjugate gradient method in AO basis.

3. COMPUTATIONAL DETAILS

We implemented the calculation of normal Raman activities for both RHF and UHF formulations of FMO in GAMESS[72,73] and parallelized it with the generalized distributed data interface (GDDI).[74] FragIt program was used for making FMO input files.[75] In order to analyze Raman spectra, intense Raman active normal modes were localized by the unitary transformation method,[76] and the respective transformed vibrational modes and their frequencies were used as for the peak assignment. We note that the localization method very slightly changes some frequencies: for instance, in crambin, the deviations were 0−6 cm^{-1}. The unitary transformations were performed with Movipac program.[77]

The accuracy of FMO-HF is evaluated in comparison with full HF calculations. For this purpose, the following three systems were used: vitamin C solvated in 30 water molecules as a test of FMO-RHF, TEMPO solvated in *N,N*-dimethylformamide (DMF) as a test of FMO-UHF, and α-tocopherol (vitamin E) as a test of FMO-RHF with fragments connected by covalent bonds (see Figure 1 for the fragmentation details). The computational efficiency is demonstrated on box-shaped water clusters, with the linear box sizes from 5 to 17 Å (from 24 to 495 atoms). For applications, we calculated a polystyrene oligomer and crambin (PDB code: 1CRN),[67] with 223 and 642 atoms, respectively.

We used the default values of various thresholds. For the numeric second derivative of the dispersion energy, we did double differencing with the offset of 10^{-6} au, while for the numeric derivatives of the gradient with respect to the electric field we used double differencing with the offset of 0.002 au. For the separated dimer approximation[78] we used the threshold of 2.0 (it is unitless, because it is applied to unitless distances computed as the usual values divided by the sum of the atomic van der Waals radii). All geometries were optimized with the geometry convergence threshold OPTTOL of 10^{-4} hartree/bohr. For all calculations we used the 6-31G(d) basis set with spherical harmonics (ISPHER = 1), and the Grimme's dispersion model[63] was employed to consider the dispersion contributions. The geometry optimization of crambin was performed with the polarizable continuum model (PCM)[79,80] using the default PCM settings at the FMO-PCM⟨1⟩ level.[80]

TEMPO solvated in explicit DMF molecules is fragmented as one molecule per fragment, while two water molecules are merged into one fragment for vitamin C solvated in explicit water. This was done according to the pair interaction energies (PIE) in FMO,[81] by merging the pair with the largest PIE first, then the second largest and so on. The fragmentation pattern of vitamin C is shown in Figure 1.

We used the Gaussian broadening in the IR and Raman spectra simulations. The contribution of mode *i* to the IR intensity *I* (and likewise Raman activity) is calculated as

$$I(\omega) = \frac{I_i}{\eta} \exp\left[-\left(\frac{\omega - \omega_i}{\eta}\right)^2\right] \tag{37}$$

where I_i and ω_i are the IR intensity and frequency for the normal vibrational mode *i*, and η is the broadening parameter for the line width (10 cm^{-1} is used throughout this study).

4. RESULTS AND DISCUSSION

4.1. FMO Accuracy. The results shown in Figure 2 demonstrate the FMO-HF accuracy in comparison with full HF
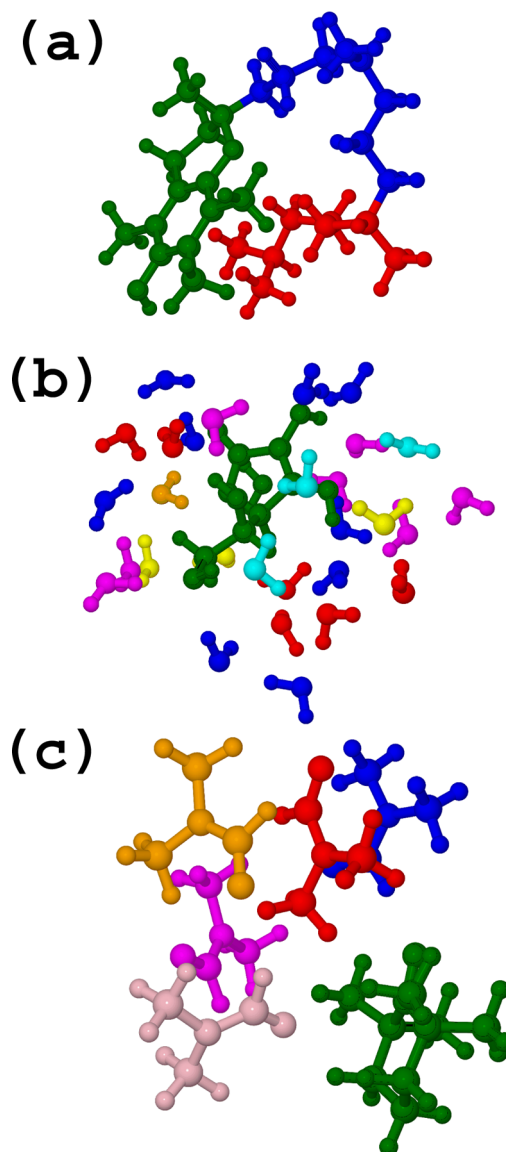

Figure 1. Fragmentation of the molecular systems, showing fragments in different colors. (a) vitamin E, (b) vitamin C solvated in water, and (c) TEMPO solvated in DMF.

calculations for vitamin C solvated in water molecules, α-tocopherol, and TEMPO solvated in DMF. Among all normal modes, the maximum FMO-HF deviation from full HF for vitamin C, α-tocopherol, and TEMPO is 27.1, 6.2, and 7.1 cm^{-1}, respectively, while rmsd is 8.9, 1.3, and 1.1 cm^{-1}, respectively.

For vitamin C the hydrogen bonding brings in many-body quantum effects (e.g., the three-body charge transfer, exchange-repulsion, and their coupling for two hydrogen bonds involving three fragments), which are not accounted for in FMO2. These effects tend to increase the errors, which are especially large for vibrational modes delocalized over several water molecules, coupled with OH in vitamin C. Likewise, the maximum errors in α-tocopherol and TEMPO are found in the delocalized vibrational modes.

A summary of the intense Raman modes is given in Table 1 (we note that the values correspond to individual vibrational modes from the Hessian calculations). The errors in frequencies are 2.1, 0.2, and 0.2 cm^{-1} in vitamin C, vitamin

(a)

(b)

(c)
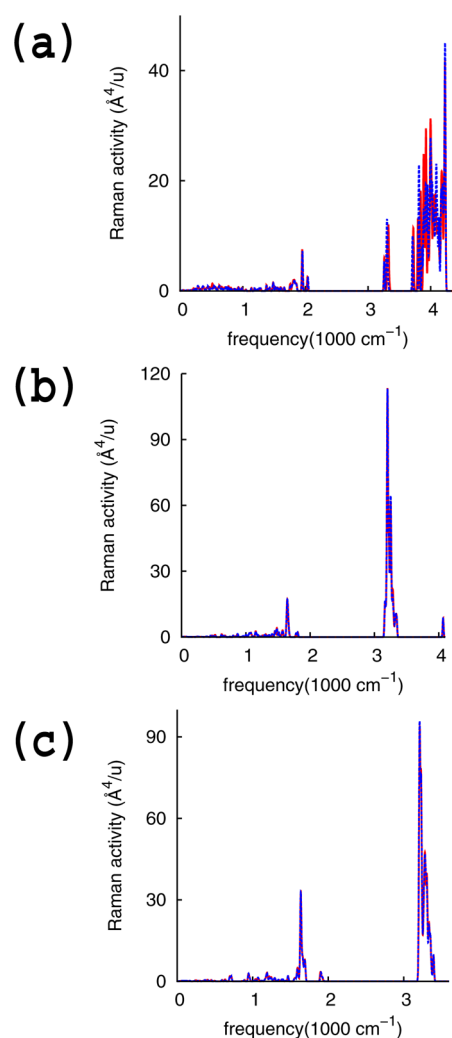
Figure 2. Raman spectra calculated with FMO-HF and full HF, shown with red solid and blue dashed lines, respectively. (a) Vitamin C solvated in water, (b) vitamin E, and (c) TEMPO solvated in DMF. See SI for detailed numeric results.

Table 1. Frequencies (cm^{-1}) and Raman Activities (Å^4/u) for Prominent Modes of the Solute in Vitamin C, α-Tocopherol, and TEMPO, Computed with FMO-HF and full HF using the 6-31G(d) Basis Set

	vibration		Raman activity	
system	FMO-HF	HF	FMO-HF	HF
vitamin C[a]	3884.5	3886.6	150.4	144.9
vitamin E[a]	3203.8	3204.0	403.2	369.9
TEMPO[b]	3237.2	3237.4	130.6	124.0

[a]Singlet with RHF. [b]Doublet with UHF.

E, and TEMPO, respectively, while the errors in the Raman activities are 5.5, 33.3, and 6.6 Å^4/u, respectively.

4.2. Analysis of the Raman Spectrum of a Polystyrene Oligomer. Raman and IR spectra of a polystyrene oligomer, divided into two units per fragment, are shown in Figure 3. In order to analyze these spectra, we localized the vibrational modes using the unitary transformation method[76] for the polystyrene oligomer divided into the head (reaction center), body (middle part), or tail (capped with Phe-COO) domains. The Raman active vibrational peaks can be divided into the

low- (450−1600 cm^{-1}) and high-frequency (2864−3044 cm^{-1}) regions. The localization analysis clearly shows that these two regions are delocalized and localized, respectively.

The vibrational modes in the low-frequency region (450−1000 cm^{-1}) describe C−C backbone stretching, and C−H bending of the backbone CH$_2$ groups. They are delocalized over the entire system, and it is not meaningful to decompose these modes into the three domains.

On the other hand, the high-frequency region (2864−3044 cm^{-1}), corresponding to the C−H stretching in phenyl groups or the backbone, can be analyzed. The results of the analysis are for a selection of normal modes representing several important peaks are shown in Figure 3c,d. The vibrational modes for the C−H backbone stretching are very clearly divided between the terminal domains (head and tail) and the body domain. The vibrational modes localized in the terminal domains have the vibrational frequencies in the middle range (from 2872 to 2913 cm^{-1}), whereas the body domain has the frequencies in the ranges of 2870−2872 and 2913−2918 cm^{-1} (except of one mode of 2870 cm^{-1}, localized on the head domain). Comparing the terminal domains, more active modes are localized in the head.

For the C−H stretching in phenyl groups one can also observe a distinctly different localization on either the body or terminal domains, with the exception of some modes with comparable localization factors. Also, in general many active vibrational modes of phenyl C−H vibrations are localized on the body domain with small or negligible contributions from the terminal domains. The coupling of vibrations of the body and terminal domains observed for some modes may be important for analyzing measured polymer spectra.

We note that the localization analysis in general can only provide a qualitative assignment. Most vibrational modes do have contributions from all three domains; however, for the C−H stretching it is often possible to identify the main contributor. Summarizing, the main benefit of the localization analysis is the ability to label individual peaks by the geometric domain (head, body, or tail) for localized modes.

4.3. IR and Raman Spectra of Crambin. Crambin is composed of two α-helices and one β-turn; this protein is relatively rigid due to three disulfide bonds, and it was studied with various theoretical methods.[82−88] Some information about the secondary structure of proteins can be obtained from the amide I band in Raman spectra.[89] We note that because of peak broadening, a single peak corresponds to a number of vibrational modes in the nearest vicinity of the main frequency, which has the highest intensity.

Using FMO/PCM, we optimized the structure of crambin solvated in water (all atoms). The optimized geometry superimposed on the X-ray (PDB: 1CRN) crystal structure in Figure 4 shows their reasonable agreement, with the rmsd from experiment of 0.5249 Å.

For the optimized structure we calculated both IR and Raman spectra of crambin, shown in Figure 5a. In the IR spectrum, both Amide I and II (N−H bending coupled with C−N stretch) bands have high intensities. In the Raman spectrum, the CH$_3$ stretching mode has prominent peaks in addition to the less intense Amide I band, while the Raman activity of the Amide II band is very small. A comparison of the calculated and experimental Raman peaks is given in Table 2, while IR peaks are summarized in Table 3. The CH$_3$ stretching peaks from FMO calculations are 1412 and 1474 cm^{-1}, whereas the Amide I peaks are 1645 and 1687 cm^{-1}. The experimentally
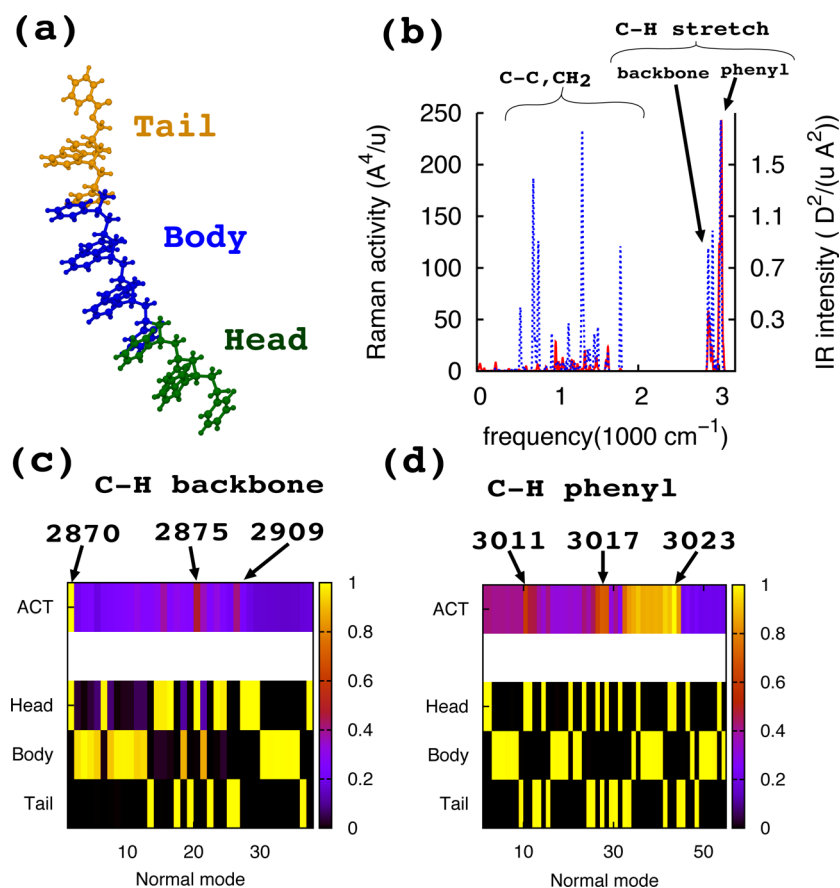
Figure 3. (a) Fragmentation of the polystyrene oligomer. (b) Normal Raman spectrum (red solid line), and IR spectrum (blue dashed line), calculated with FMO-RHF/6-31G(d). Analysis of some selected localized vibrational modes for C–H stretching in (c) the backbone and (d) phenyl groups. Normal modes are numbered in the order of increasing frequencies, some of which in cm^{-1} are shown above the activity bar. The color bar on the top (act) represents relative Raman activity (the fraction of 1.0, shown as yellow, is the highest peak; other peaks are shown as fractions of the highest peak). The color bar on the right (with numbers from 0 to 1) shows the color scheme used both for activities (act) and fractions of the domains to the given vibrational mode. For instance the smallest shown frequency in (c) is colored yellow for "head" and black for the rest, which means that the head is the main component for that vibration, whereas the activity on the top is yellow, which indicates that this is the highest peak (the largest activity). Frequencies are scaled[91] by 0.8953 for comparison with experiment.

Crambin (1CRN)
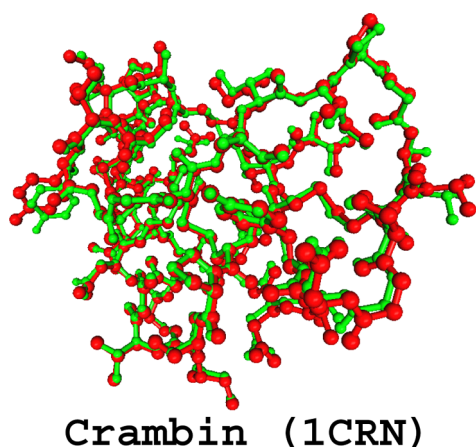
Figure 4. Superimposed crambin structures obtained with FMO-RHF/D/PCM/6-31G(d) (red) on the X-ray experiment[67] (green). The rmsd between them is 0.5249 Å.

obtained[90] peaks are 1410, 1480, 1610, and 1660 cm^{-1}, in good agreement with our calculations.

To assign domains in Figure 5b to observed Raman peaks, we applied the localization analysis. The results for selected

CH$_3$ and Amide I bands are shown in Figure 5c,d, respectively. The CH$_3$ stretching peak at 1412 cm^{-1} (not shown) is attributed to the α-Helices A and B and the β-sheet, whereas the most intense CH$_3$ stretching peak at 1474 cm^{-1} is attributed mainly to the α-Helix A with a small contribution from the α-Helix B. For the Amide I band, the 1645 cm^{-1} peak is delocalized over the whole protein, whereas the 1687 cm^{-1} peak is mainly due to the α-Helix A.

4.4. Computational Timing. The computational efficiency is shown for the box-shaped cluster of water molecules, with the linear box sizes of 5.0, 8.0, 13.5, 16.0, and 17.0 Å containing 24, 93, 249, 408, and 495 atoms, respectively. The timings were measured on 16 nodes equipped with 2.93 GHz Xeons (8 CPU cores and 12 GB memory per node). The computational timings for calculating Raman activities are shown in Figure 6 (these numbers do not include the Hessian timings).

It can be seen that the scaling of FMO is considerably lower than that of full RHF. For the largest system containing 495 atoms, FMO-RHF and full RHF took 2.1 and 6.4 h, respectively.

We note that the most expensive step for Raman simulations is not the calculation of the derivatives of the polarizability tensor α but the Hessian calculation to obtain the normal coordinates and vibrational frequencies.[50] For crambin the
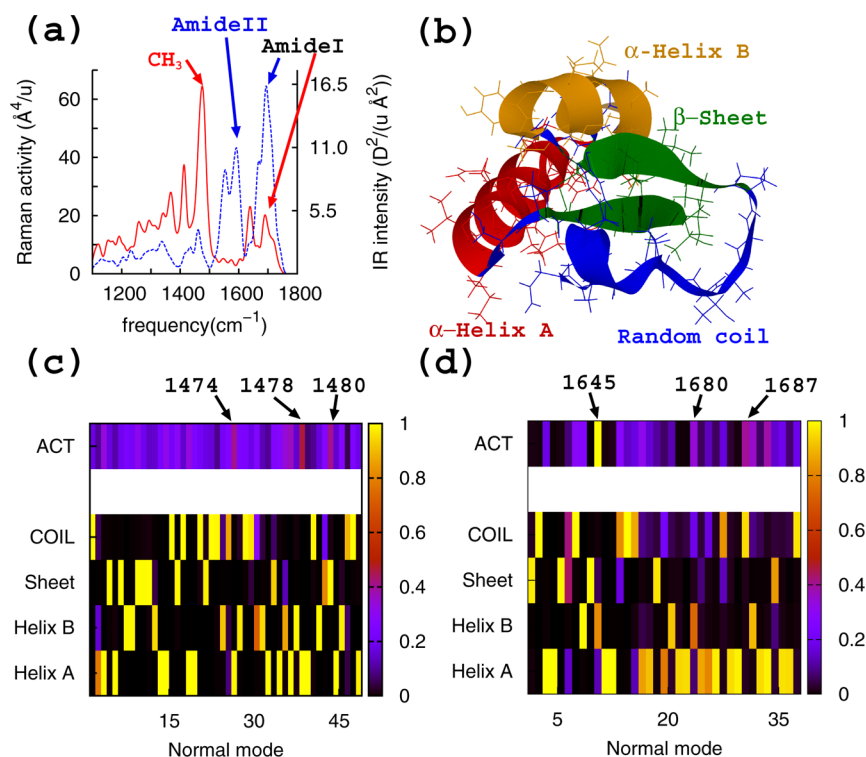
Figure 5. (a) Calculated Raman (red solid line) and IR (blue dashed line) spectra of crambin. The frequency is scaled by 0.8953 for better comparison to experiment. (b) Schematic illustration of crambin showing the domains. Domain contributions to Raman activities for (c) CH_3 and (d) Amide I bands. The color bar on the top (act) represents relative Raman activity (the fraction of 1.0, shown as yellow, is the highest peak; other peaks are shown as fractions of the highest peak). Normal modes are numbered in the order of increasing frequencies, some of which in cm^{-1} are shown above the activity bar. The color bar on the right (with numbers from 0 to 1) shows the color scheme used both for activities (act) and fractions of the domains to the given vibrational mode. For instance the smallest shown frequency in (c) is colored yellow for "COIL" and black for the rest, which means that the coil is the main component for that vibration, whereas the activity on the top is purple, which indicates a relatively small value. Helix, sheet, and COIL denote the α-helix, β-sheet and random coil, respectively.

Table 2. Prominent Raman Peaks (cm^{-1}) in Crambin Calculated with FMO-RHF/D/6-31(d) and Measured in Experiment^a (ref 90)

|	CH$_3$		amide I	
FMO	1412	1475	1639	1690
FMO^b	1412	1474	1645	1687
experiment	1410	1480	1610	1660

^{a}The computed spectrum is shown in Figure 5a. The calculated frequencies are scaled[91] by 0.8953. ^{b}After applying the localization transformation.

Table 3. Prominent IR Peaks (cm^{-1}) in Crambin Calculated with FMO-RHF/D/6-31(d)^a

type	frequency	intensity
amide II-1	1554	9.1
amide II-2	1591	11.1
amide I-1	1668	9.9
amide I-2	1694	16.5

^{a}The computed spectrum is shown in Figure 5a. The frequencies are scaled[91] by 0.8953.

Hessian and Raman activity calculations took 53 and 26 h, respectively (using 25 Xeon nodes, 228 CPU cores in total). The FMO methods significantly reduces both memory requirements and computational cost and enables large scale simulations of IR and Raman spectra.
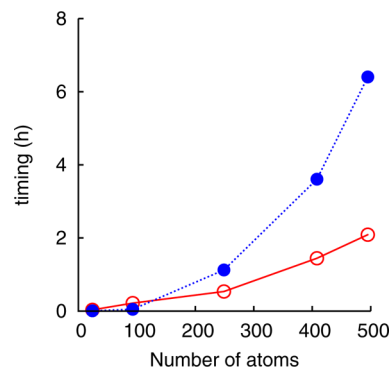
Figure 6. Timings of Raman activity calculations for box-shaped clusters of water molecules, depicted for FMO-RHF and RHF with red solid and blue dotted lines, respectively (measured on 16 nodes with 2.93 GHz Xeons, equipped with 8 CPU cores and 12 GB RAM per node). 6-31G(d) is used.

5. CONCLUSIONS

We have developed a method to calculate Raman activities in the framework of the fragment molecular orbital, implemented in GAMESS and parallelized using GDDI. In addition, we have also developed analytic and numeric second derivatives for the Grimme's dispersion models.[62,63] We have shown that Raman activities calculated with FMO are in reasonable agreement with full HF results, for a number of representative closed-shell and radical systems.

As an application of the developed method, we have calculated IR and Raman spectra of a polystyrene oligomer and a small protein, crambin. We have also optimized the structure of crambin using FMO and reproduced the experimental X-ray structure with rmsd of 0.5249 Å. The experimental Raman spectrum of crambin is in good agreement with our calculated results. By the application of the vibrational mode localization analysis we have assigned calculated peaks to particular geometric domains, which is possible for many but not all modes, because some of them are delocalized over the whole system. The delocalization effects in FMO2 are accounted for with pairwise corrections from fragment dimers, however some limitations to the accuracy are imposed by the treatment of delocalized modes in this way.

FMO calculations of Raman spectra are considerably faster than full HF calculations, and they also require much less memory. The Raman activity calculation of crambin (642 atoms) took 115 MB of memory per core and 26.5 h using 25 Xeon nodes (228 CPU cores in total). The Hessian and IR calculation of crambin took 2204 MB of memory per core and 53 h on the same cluster. FMO can be applied to simulate Raman and IR spectra of realistic polymers with defects, irregular, and amorphous structures, and the observed peaks can be assigned based on their normal coordinates.

■ ASSOCIATED CONTENT

Ⓢ Supporting Information

Detailed derivations of the second derivatives for the dispersion model; tables of Raman peaks computed with FMO-HF and HF for vitamins C and E and TEMPO; and IR and Raman peaks computed with FMO for the polystyrene oligomer. This material is available free of charge via the Internet at http://pubs.acs.org.

■ AUTHOR INFORMATION

Corresponding Authors
*E-mail: nakata.h.ab@m.titech.ac.jp.
*E-mail: d.g.fedorov@aist.go.jp.

Notes
The authors declare no competing financial interest.

■ ACKNOWLEDGMENTS

■ REFERENCES

(1) Kim, H.; Cho, M. *Chem. Rev.* **2013**, *113*, 5817−5847.
(2) Vass, E.; Hollósi, M.; Besson, F.; Buchet, R. *Chem. Rev.* **2003**, *103*, 1917−1954.
(3) Ferraro, J. R., Nakamoto, K., Eds. *Introductory Rraman Spectroscopy*; Academic Press: London, 1994.
(4) Deglmann, P.; Furche, F.; Ahlrichs, R. *Chem. Phys. Lett.* **2002**, *362*, 511−518.
(5) Alexeev, Y.; Schmidt, M. W.; Windus, T. L.; Gordon, M. S. *J. Comput. Chem.* **2007**, *28*, 1685−1694.
(6) Pulay, P. *Mol. Phys.* **1969**, *17*, 197−204.
(7) Warshel, A.; Karplus, M. *J. Am. Soc. Chem.* **1972**, *94*, 5612−5625.
(8) Cui, Q.; Karplus, M. *J. Chem. Phys.* **2000**, *112*, 1133−1149.
(9) Dapprich, S.; Komáromi, I.; Byun, K. S.; Morokuma, K.; Frisch, M. J. *J. Mol. Struct.: THEOCHEM* **1999**, *461*, 1−21.
(10) Witek, H. A.; Irle, S.; Morokuma, K. *J. Chem. Phys.* **2004**, *121*, 5163−5170.
(11) Zheng, W.; Brooks, B. R. *Biophys. J.* **2005**, *89*, 167−178.
(12) Li, H.; Jensen, J. H. *Theor. Chem. Acc.* **2002**, *107*, 211−219.
(13) Ghysels, A.; Van Neck, D.; Van Speybroeck, V.; Verstraelen, T.; Waroquier, M. *J. Chem. Phys.* **2007**, *126*, 224102.
(14) Komornicki, A.; McIver, J. W. *J. Chem. Phys.* **1979**, *70*, 2014−2016.
(15) Bacskay, G. B.; Saebø, S.; Taylor, P. R. *Chem. Phys.* **1984**, *90*, 215−224.
(16) Johnson, B. G.; Florian, J. *Chem. Phys. Lett.* **1995**, *247*, 120−125.
(17) Stirling, A. *J. Chem. Phys.* **1996**, *104*, 1254−1262.
(18) Jalkanen, K.; Degtyarenko, I.; Nieminen, R.; Cao, X.; Nafie, L.; Zhu, F.; Barron, L. *Theor. Chem. Acc.* **2008**, *119*, 191−210.
(19) Ramnarayan, K.; Bohr, H.; Jalkanen, K. *Theor. Chem. Acc.* **2008**, *119*, 265−274.
(20) Jürgensen, V. W.; Jalkanen, K. *Phys. Biol.* **2006**, *3*, S63−S79.
(21) Nikitina, E.; Sulimov, V.; Zayets, V.; Zaitseva, N. *Int. J. Quantum Chem.* **2004**, *97*, 747−763.
(22) Stewart, J. J. P. *J. Mol. Model.* **2009**, *15*, 765−805.
(23) Goedecker, S.; Scuseria, G. E. *Comp. Sci. Eng.* **2003**, *5*, 14−21.
(24) *Linear-Scaling Techniques in Computational Chemistry and Physics*; Zalesny, R., Papadopoulos, M. G., Mezey, P. G., Leszczynski, J., Eds.; Springer: New York, 2011.
(25) Gordon, M. S.; Fedorov, D. G.; Pruitt, S. R.; Slipchenko, L. V. *Chem. Rev.* **2012**, *112*, 632−672.
(26) Otto, P.; Ladik, J. *Chem. Phys.* **1975**, *8*, 192−200.
(27) Gao, J. L. *J. Phys. Chem. B* **1997**, *101*, 657−663.
(28) Kobayashi, M.; Nakai, H. *J. Chem. Phys.* **2013**, *138*, 044102.
(29) He, X.; Merz, K. M. *J. Chem. Theory Comput.* **2010**, *6*, 405−411.
(30) Yu, H.; Leverentz, H. R.; Bai, P.; Siepmann, J. I.; Truhlar, D. G. *J. Phys. Chem. Lett.* **2014**, *5*, 660−670.
(31) Tong, Y.; Mei, Y.; Zhang, J. Z. H.; Duan, L. L.; Zhang, Q. G. *J. Theor. Comput. Chem.* **2009**, *8*, 1265.
(32) Söderhjelm, P.; Kongsted, J.; Ryde, U. *J. Chem. Theory Comput.* **2010**, *6*, 1726−1737.
(33) Gao, J.; Wang, Y. *J. Chem. Phys.* **2012**, *136*, 071101.
(34) Collins, M. A. *Phys. Chem. Chem. Phys.* **2012**, *14*, 7744−7751.
(35) Frank, A.; Möller, H. M.; Exner, T. E. *J. Chem. Theory Comput.* **2012**, *8*, 1480−1492.
(36) Gordon, M. S.; Smith, Q. A.; Xu, P.; Slipchenko, L. V. *Annu. Rev. Phys. Chem.* **2013**, *64*, 553−578.
(37) Kiewisch, K.; Jacob, C. R.; Visscher, J. *J. Chem. Theory Comput.* **2013**, *9*, 2425−2440.
(38) Rahalkar, A. P.; Ganesh, V.; Gadre, S. R. *J. Chem. Phys.* **2008**, *129*, 234101.
(39) Hua, W.; Fang, T.; Li, W.; Yu, J.-G.; Li, S. *J. Phys. Chem. A* **2008**, *112*, 10864−10872.
(40) Sakai, S.; Morita, S. *J. Phys. Chem. A* **2005**, *109*, 8424−8429.
(41) Howard, J. C.; Tschumper, G. S. *J. Chem. Phys.* **2013**, *139*, 184113.
(42) Nakata, H.; Nagata, T.; Fedorov, D. G.; Yokojima, S.; Kitaura, K.; Nakamura, S. *J. Chem. Phys.* **2013**, *138*, 164103.
(43) Kitaura, K.; Ikeo, E.; Asada, T.; Nakano, T.; Uebayasi, M. *Chem. Phys. Lett.* **1999**, *313*, 701−706.
(44) *The Fragment Molecular Orbital Method: Practical Applications to Large Molecular Systems*; Fedorov, D. G., Kitaura, K., Eds.; CRC press: Boca Raton, FL, 2009.
(45) Fedorov, D. G.; Kitaura, K. *J. Phys. Chem. A* **2007**, *111*, 6904−6914.
(46) Fedorov, D. G.; Nagata, T.; Kitaura, K. *Phys. Chem. Chem. Phys.* **2012**, *14*, 7562−7577.
(47) Tanaka, S.; Mochizuki, Y.; Komeiji, Y.; Okiyama, Y.; Fukuzawa, K. *Phys. Chem. Chem. Phys.* **2014**, *16*, 10310−10344.

(48) Nagata, T.; Brorsen, K.; Fedorov, D. G.; Kitaura, K.; Gordon, M. S. *J. Chem. Phys.* **2011**, *134*, 124115.

(49) Nagata, T.; Fedorov, D. G.; Kitaura, K. *Chem. Phys. Lett.* **2012**, *544*, 87−93.

(50) Nakata, H.; Fedorov, D. G.; Yokojima, S.; Kitaura, K.; Nakamura, S. *Chem. Phys. Lett.* **2014**, *603*, 67.

(51) Mochizuki, Y.; Ishikawa, T.; Tanaka, K.; Tokiwa, H.; Nakano, T.; Tanaka, S. *Chem. Phys. Lett.* **2006**, *418*, 418−422.

(52) Mazanetz, M. P.; Ichihara, O.; Law, R. J.; Whittaker, M. *J. Cheminf.* **2011**, *3*, 2.

(53) Sawada, T.; Fedorov, D. G.; Kitaura, K. *J. Am. Chem. Soc.* **2010**, *132*, 16862−16872.

(54) Watanabe, T.; Inadomi, Y.; Fukuzawa, K.; Nakano, T.; Tanaka, S.; Nilsson, L.; Nagashima, U. *J. Phys. Chem. B* **2007**, *111*, 9621−9627.

(55) Fedorov, D. G.; Avramov, P. V.; Jensen, J. H.; Kitaura, K. *Chem. Phys. Lett.* **2009**, *477*, 169−175.

(56) Carlson, P. J.; Bose, S.; Armstrong, D. W.; Hawkins, T.; Gordon, M. S.; Petrich, J. W. *J. Phys. Chem. B* **2012**, *116*, 503−512.

(57) Avramov, P. V.; Fedorov, D. G.; Sorokin, P. B.; Sakai, S.; Entani, S.; Ohtomo, M.; Y. Matsumoto, H. N. *J. Phys. Chem. Lett.* **2012**, *3*, 2003−2008.

(58) Okiyama, Y.; Tsukamoto, T.; Watanabe, C.; Fukuzawa, K.; Tanaka, S.; Mochizuki, Y. *Chem. Phys. Lett.* **2013**, *566*, 25−31.

(59) Roskop, L.; Fedorov, D. G.; Gordon, M. S. *Mol. Phys.* **2013**, *111*, 1622−1629.

(60) Nakata, H.; Fedorov, D. G.; Nagata, T.; Yokojima, S.; Ogata, K.; Kitaura, K.; Nakamura, S. *J. Chem. Phys.* **2012**, *137*, 044110.

(61) Nakata, H.; Fedorov, D. G.; Yokojima, S.; Kitaura, K.; Nakamura, S. *Theor. Chem. Acc.* **2014**, *1477*, 133.

(62) Grimme, S. *J. Comput. Chem.* **2006**, *27*, 1787−1799.

(63) Grimme, S.; Antony, J.; Ehrlich, S.; Krieg, H. *J. Chem. Phys.* **2010**, *132*, 154104.

(64) Yamaguchi, Y.; Schaefer, H. F., III; Osamura, Y.; Goddard, J. *A New Dimension to Quantum Chemistry: Analytical Derivative Methods in Ab Initio Molecular Electronic Structure Theory*; Oxford University Press: New York, 1994.

(65) Wang, Y.; Tominaga, Y. *J. Phys. Soc. Jpn.* **1993**, *62*, 4198−4201.

(66) Cai, T.; Gu, H.; Liu, F.; Xie, M. *Appl. Spectrosc.* **2012**, *66*, 114−121.

(67) Teeter, M. M. *Proc. Nat. Acad. Sci. U.S.A.* **1984**, *81*, 6014−6018.

(68) Fedorov, D. G.; Kitaura, K. *J. Chem. Phys.* **2004**, *120*, 6832−6840.

(69) Nakano, T.; Mochizuki, Y.; Yamashita, K.; Watanabe, C.; Fukuzawa, K.; Segawa, K.; Okiyama, Y.; Tsukamoto, T.; Tanaka, S. *Chem. Phys. Lett.* **2012**, *523*, 128−133.

(70) Grimme, S. *J. Comput. Chem.* **2006**, *27*, 1787−1799.

(71) Nagata, T.; Fedorov, D. G.; Kitaura, K. *Chem. Phys. Lett.* **2010**, *492*, 302−308.

(72) Schmidt, M. W.; Baldridge, K. K.; Boatz, J. A.; Elbert, S. T.; Gordon, M. S.; Jensen, J. H.; Koseki, S.; Matsunaga, N.; Nguyen, K. A.; Su, S.; Windus, T. L.; Dupuis, M.; Montgomery, J. A. *J. Comput. Chem.* **1993**, *14*, 1347−1363.

(73) Gordon, M. S.; Schmidt, M. W. In *Theory and Applications of Computational Chemistry, the first forty years*; Dykstra, C. E., Frenking, G., Kim, K. S., Scuseria, G. E., Eds.; Elsevier: Amsterdam, 2005; pp 1167−1189.

(74) Fedorov, D. G.; Olson, R. M.; Kitaura, K.; Gordon, M. S.; Koseki, S. *J. Comput. Chem.* **2004**, *25*, 872−880.

(75) Steinmann, C.; Ibsen, M. W.; Hansen, A. S.; Jensen, J. H. *PLoS One* **2012**, *7*, e44480.

(76) Jacob, C. R.; Luber, S.; Reiher, M. *J. Phys. Chem. B* **2009**, *113*, 6558−6573.

(77) Weymuth, T.; Haag, M. P.; Kiewisch, K.; Luber, S.; Schenk, S.; Jacob, C. R.; Herrmann, C.; Neugebauer, J.; Reiher, M. *J. Comput. Chem.* **2012**, *33*, 2186−2198.

(78) Fedorov, D. G.; Ishida, T.; Uebayasi, M.; Kitaura, K. *J. Phys. Chem. A* **2007**, *111*, 2722−2732.

(79) Li, H.; Fedorov, D. G.; Nagata, T.; Kitaura, K.; Jensen, J. H.; Gordon, M. S. *J. Comput. Chem.* **2010**, *31*, 778−790.

(80) Nagata, T.; Fedorov, D. G.; Li, H.; Kitaura, K. *J. Chem. Phys.* **2012**, *136*, 204112.

(81) Fedorov, D. G.; Kitaura, K. *J. Comput. Chem.* **2007**, *28*, 222−237.

(82) Van Alsenoy, C.; Yu, C.-H.; Peeters, A.; Martin, J. M. L.; Schäfer, L. *J. Phys. Chem. A* **1998**, *102*, 2246−2251.

(83) Stewart, J. J. P. *J. Mol. Struct.: THEOCHEM* **1997**, *401*, 195−205.

(84) Exner, T. E.; Mezey, P. G. *Phys. Chem. Chem. Phys.* **2005**, *7*, 4061−4069.

(85) Ogawa, T.; Kurita, N.; Sekino, H.; Kitao, O.; Tanaka, S. *Chem. Phys. Lett.* **2004**, *397*, 382−387.

(86) van der Vaart, A.; Suarez, D.; Merz, K. M. *J. Chem. Phys.* **2000**, *113*, 10512.

(87) Ritchie, J. P. *Chem. Phys. Lett.* **2004**, *387*, 243−246.

(88) Kästner, J.; Thiel, S.; Senn, H. M.; Sherwood, P.; Thiel, W. *J. Chem. Theory Comput.* **2007**, *3*, 1064−1072.

(89) Tuma, R. *J. Raman Spectrosc.* **2005**, *36*, 307−319.

(90) Williams, R. W.; Teeter, M. M. *Biochemistry* **1984**, *23*, 6796−6802.

(91) Scott, A. P.; Radom, L. *J. Phys. Chem.* **1996**, *100*, 16502−16513.